metals

MDPI

Article

Effect of Nb on Solidification Cracking, Mechanical Properties and Corrosion Resistance of 310S Austenitic Stainless-Steel Welded Joints

Yulu Su [1], Dan Wang [2,*] and Xulei Wu [1]

[1] School of Materials Science and Engineering, Jiangsu University of Science and Technology, Zhenjiang 212100, China
[2] School of Materials Science and Engineering, Jiangsu University, Zhenjiang 212013, China
* Correspondence: wdd_wan@ujs.edu.cn

Abstract

In this study, 310S austenitic stainless-steel was welded using a laser with varying amounts of Nb to systematically investigate the effect of Nb on solidification cracking susceptibility, mechanical properties, and corrosion resistance of the weld. Under the present experimental conditions, the critical restraint width was higher for the 0.58 wt.% Nb and 1.45 wt.% Nb welds than for the Nb-free and 2.3 wt.% Nb welds, indicating that Nb addition affected the solidification cracking response of the weld. At low-to-moderate Nb contents, Nb can aggravate compositional segregation and increase the presence of low-melting-point liquid films, thereby increasing cracking susceptibility. At higher Nb contents, the reduced cracking susceptibility was accompanied by microstructural refinement and changes in the distribution of Nb-rich constituents during solidification. With increasing Nb content, the number of precipitated phases in the weld increases, mainly distributed at the austenite grain boundaries in granular, elongated, and chain-like forms. The introduction of Nb generally increases the microhardness and tensile strength of the welded joint, attributed to grain refinement strengthening and solid-solution strengthening. The reduction in area first increased and then decreased, suggesting that excessive Nb addition may reduce ductility because of the increased amount of grain-boundary precipitates and local strengthening heterogeneity. With increasing Nb content, the Ir/Ia ratio decreased from 67.6% to 52.2%, suggesting improved intergranular corrosion resistance. This improvement is likely related to the preferential reaction of Nb with carbon, which may suppress the formation of Cr-depleted zones at grain boundaries. Overall, Nb addition improved the corrosion resistance and increased the hardness and tensile strength of the weld; however, its effect on solidification cracking susceptibility was non-monotonic, indicating that careful control of Nb content is required to balance cracking susceptibility, mechanical properties, and corrosion resistance.

Academic Editor: Dariusz Rozumek

Received: 31 March 2026
Revised: 29 April 2026
Accepted: 16 May 2026
Published: 19 May 2026

Keywords: stainless-steel; laser welding; niobium (Nb); solidification cracks; mechanical properties; corrosion resistance

1. Introduction

Austenitic stainless-steels are widely used in the manufacturing industry owing to their excellent corrosion resistance, high-temperature capability, and good formability [1,2]. The fabrication and service of various products and structural components inevitably rely on welding technologies. With the continuous advancement of manufacturing, laser

welding—compared with conventional arc welding—has demonstrated distinct advantages, including high welding efficiency, low heat input, small welding-induced distortion, and easy automation. Consequently, laser welding has been extensively applied in automotive manufacturing [3,4], shipbuilding [5], transportation equipment [6,7], aerospace [8], and petro-chemical engineering [9], as well as in the welding of transparent materials for microdevices [10,11].

The performance of welded joints directly affects the service safety and lifetime of products and structures, and weld-metal chemistry design is one of the key factors for achieving high-performance joints [12]. To improve the overall properties of austenitic stainless-steel welds, microalloying is commonly employed to tailor the weld-metal composition, in which Nb is a frequently used strengthening element. The addition of Nb can enhance the mechanical properties and high-temperature performance of welds through grain-refinement strengthening, precipitation strengthening, and solid-solution strengthening. In addition, Nb can improve the corrosion resistance of austenitic stainless-steel welds by preferentially combining with carbon, suppressing the formation of Cr-depleted zones at grain boundaries, and potentially modifying the stability and composition of the passive film. However, for austenitic stainless-steel welds, Nb may also promote the formation of low-melting Nb-rich liquid films along grain boundaries, thereby increasing the susceptibility to solidification cracking. Therefore, how to balance the effects of Nb on solidification cracking susceptibility, corrosion resistance, and joint mechanical properties to achieve multi-property optimization remains to be further investigated.

Previous studies have shown that alloying elements significantly influence solidification cracking behavior in austenitic stainless-steel welds. Seidai et al. [13] investigated the effects of Nb, Ti, and Zr on solidification cracking susceptibility using a transverse adjustable restraint test. The results indicated that the solidification brittle temperature range (BTR) and the maximum crack length followed the order: 2Ti (266.9 °C) > 2Zr (194.1 °C) > 2Nb (150.1 °C), suggesting that Ti exerts a more pronounced effect on solidification cracking susceptibility than Nb and Zr. Shamanian et al. [14] conducted an adjustable restraint test on dissimilar joints of Inconel 617 and 310 stainless-steel and found that using Inconel 617 as the filler metal resulted in relatively low solidification cracking susceptibility, whereas using 310 austenitic stainless-steel as the filler metal markedly increased the susceptibility. This was mainly attributed to the broadened solidification temperature range and the promoted formation of low-melting phases induced by 310 stainless-steel.

On the other hand, Nb can positively contribute to the mechanical and corrosion properties of austenitic stainless-steel joints. Nb readily forms carbo-nitrides with C and N, which can inhibit grain-boundary migration and refine austenite grains, thereby improving joint strength and overall mechanical performance [15]. Moreover, when Nb is present in solid solution in austenite, its larger atomic radius compared with Fe induces lattice distortion and impedes dislocation motion, leading to solid-solution strengthening and improved mechanical properties [16]. In terms of corrosion resistance, Nb has a higher affinity for C than Cr and thus preferentially forms carbides, suppressing the formation of Cr-depleted zones at grain boundaries [17]. It has been reported that the addition of Nb to welded joints of 06Cr18Ni11Ti austenitic stainless-steel and 15-15Ti/16-15NbSi austenitic stainless-steel can significantly enhance resistance to intergranular corrosion [18]. In addition, localized breakdown of the passive film on austenitic stainless-steels in corrosive media can readily trigger pitting corrosion [19]. By fixing C and increasing the Cr content in the passive film, Nb can raise the pitting potential and thus improve pitting corrosion resistance [20].

In summary, Nb has a dual effect on the performance of austenitic stainless-steel welds: it can improve joint mechanical properties and corrosion resistance, but it may also increase solid-

ification cracking susceptibility. Existing studies have mainly focused on conventional welding processes or on the influence of Nb on a single property. However, for 310S austenitic stainless-steel laser welds, the coupled effects of Nb content on solidification cracking susceptibility, mechanical properties, and intergranular corrosion-related behavior remain insufficiently understood. In particular, the trade-off among cracking tendency, strength–ductility response, and corrosion resistance has not been systematically established.

Therefore, this study systematically investigates the effect of Nb addition on the microstructure and performance of 310S laser welds. Rather than proposing a new characterization method, the aim of this work is to establish an integrated relationship among Nb content, microstructural evolution, solidification cracking susceptibility, mechanical response, and corrosion-related behavior under comparable welding conditions.

2. Materials and Methods

This study used SUS310S austenitic stainless-steel plates to fabricate 310S/310S butt joints with different Nb contents by introducing pure Nb foil at the butt interface to tailor the weld-metal composition. The base plates were 100 mm × 200 mm × 2 mm, and their chemical composition is listed in Table 1. The 310S plates were machined into butt-joint coupons of approximately 95 mm × 40 mm × 2 mm. To ensure a consistent specimen genealogy and comparable prior thermal histories, four precursor joint conditions were prepared using the same ultrasonic-assisted TIG (Aotai Electric Co., Ltd., Jinan, China) butt-welding route, including a 0 wt.% Nb control and three Nb-containing conditions. For the Nb-containing conditions, 0.05 mm thick Nb foils were cut into strips with widths of 1.0 mm, 2.5 mm, and 4.0 mm and placed at the joint interface before TIG welding; for the 0 wt.% Nb condition, the same joint preparation and TIG processing procedure were used, except that no Nb foil was inserted. Ultrasonic-assisted TIG butt welding was employed to melt the Nb foil into the molten pool and promote elemental diffusion, and the corresponding TIG welding parameters are summarized in Table 2. After TIG welding, all joints were ground flush to remove weld reinforcement and to obtain comparable surface conditions. The resulting TIG-fabricated precursor coupons were then divided into two branches, as illustrated in Figure 1. One branch was machined into trapezoidal specimens for laser remelting hot-cracking tests to evaluate solidification cracking susceptibility, following the method described in Refs. [21,22]. The corresponding laser (TRUMPF, Ditzingen, Germany) remelting parameters are listed in Table 3. The other branch was subjected to autogenous laser welding under identical laser parameters to produce laser welds for microstructural characterization, microhardness testing, tensile testing, and double-loop electrochemical potentiokinetic reactivation (DL-EPR) measurements. Therefore, within each comparison set, all specimens shared the same precursor fabrication route, and Nb content was the only intentional compositional variable. The autogenous laser weld was produced on the TIG-fabricated precursor coupon under identical laser parameters for all Nb levels, and the analyzed region in the present work was the laser fusion zone generated during this final laser-welding step.

Table 1. Chemical composition of stainless-steel (wt.%).

C	Si	Mn	Cr	Ni	Co	P + S	Mo	Fe
0.057	0.560	1.400	25.090	19.220	0.330	0.017	—	Bal.

Table 2. TIG welding process parameters.

Current (A)	Voltage (V)	Welding Speed (m/min)	Shielding Gas Flow Rate (Top & Back Side) (L/min)	Tungsten Electrode Diameter (mm)	Arc Length (mm)	Ultrasonic Excitation (Voltage/Frequency) (V/kHz)
106	17.7	0.2	20	2.4	~2	75/60

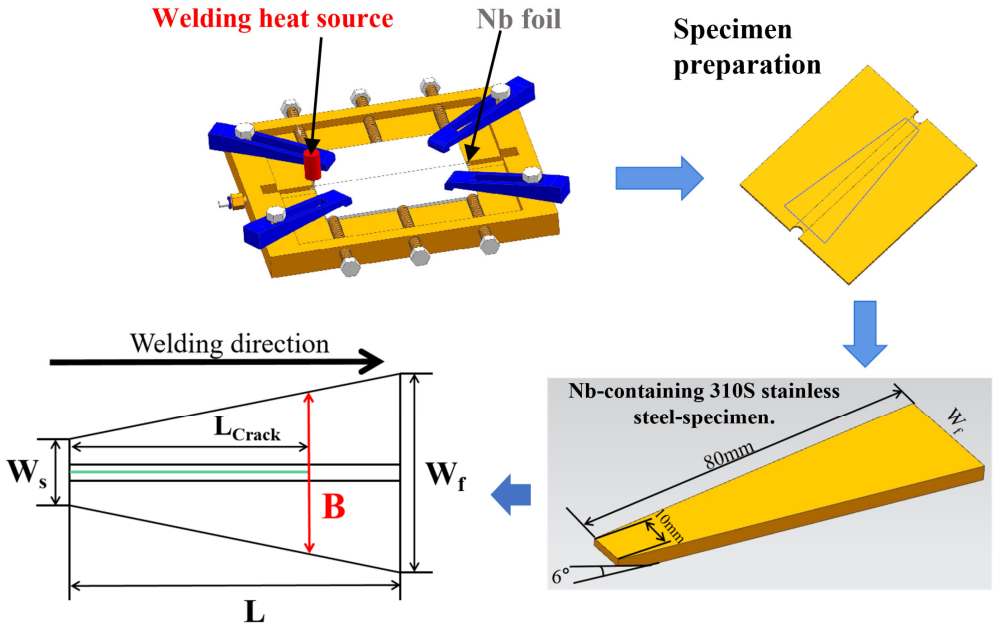

Figure 1. Preparation of Nb-containing 310S stainless-steel specimens and evaluation indexes of trapezoidal hot cracking test.

Table 3. Laser welding process parameters.

Laser Power (kW)	Defocus Distance	Welding Speed (m/min)	Argon Flow Rate (L/min)	Laser Head Tilt	Laser Wavelength (μm)	Focal Spot Diameter (mm)
1.8	0	1.0	20	~5°	1.06	~0.6

After welding, specimens were cold-mounted, ground sequentially, and polished to a mirror finish. The microstructure was revealed by electrolytic etching in a 10 wt.% oxalic acid solution at 5 V for 20–40 s. The macroscopic and microscopic morphologies of the welds were examined using a stereomicroscope (NIKON, Tokyo, Japan) and an optical microscope (Carl Zeiss AG, Jena, Germany), respectively. Weld-surface morphology and grain-boundary precipitates were characterized by SEM (FEI Nova NanoSEM 450, Hillsboro, OR, USA) and EDS (EDAX Octane Plus, Mahwah, NJ, USA). An X-ray diffractometer (XRD) (RIGAKU SmartLab, Tokyo, Japan) was employed to confirm the main phases.

Microhardness measurements were carried out on the transverse cross-sections of the welds using a Vickers hardness tester (FUTURE-TECH Corp., Kanagawa, Japan) with a load of 300 g and a dwell time of 15 s; multiple indentations were made along the cross-section to obtain hardness profiles. Room-temperature tensile tests (DDL100, DOLI company, Munich, Germany) were conducted according to GB/T 2651-2008 [23], and mechanical properties such as tensile strength and reduction in area were obtained.

Intergranular corrosion resistance was evaluated using the double-loop electrochemical potentiokinetic reactivation (DL-EPR) method through an electrochemical workstation

(Solartron Analytical, Farnborough, UK). A three-electrode cell was used. After stabilization at open-circuit potential for 5 min, the potential was scanned from −500 mV to 200 mV at 100 mV/min and then reversed back to −500 mV at the same rate. The maximum activation current (Ia) and the maximum reactivation current (Ir) were recorded, and Ir/Ia was used to characterize the degree of sensitization. The electrolyte consisted of distilled water + H_2SO_4 + KSCN, with H_2SO_4 at 3 mol/L and KSCN at 0.01 mol/L. Considering the relatively high corrosion resistance of the Nb-containing welds, the H_2SO_4 concentration was increased under the present experimental conditions to enhance the discrimination of the DL-EPR response. Because the laser welds were narrow, an exposed area of ~0.2 cm^2 was selected on the longitudinal section of the weld. The exposed area was positioned predominantly within the weld metal, while the fusion boundary and heat-affected zone were avoided as far as practicable, so as to minimize the influence of base-metal microstructural differences on the results. In the present work, the Ir/Ia values reported for the four Nb conditions are representative values obtained under identical test conditions; statistical scatter of Ir/Ia is therefore not provided in the current manuscript [24].

3. Results

3.1. Nb-Containing Welded Joints

To obtain welded joints with low, medium, and high niobium (Nb) contents, the target Nb contents in the weld metal were preset to 0.5 wt.%, 1.5 wt.%, and 2.5 wt.%, respectively. The required Nb-foil dimensions were then back-calculated using the dilution ratio relationship. Figure 2 shows the macro cross-sectional morphology of the TIG weld in 310S stainless-steel. Based on the TIG-weld cross-section, the dilution ratio was evaluated; the cross-sectional area was measured to be approximately 8.5 mm^2 using stereomicroscope images in combination with ImageJ (Version 1.53t, National Institutes of Health, Bethesda, MD, USA), as shown in Figure 2.

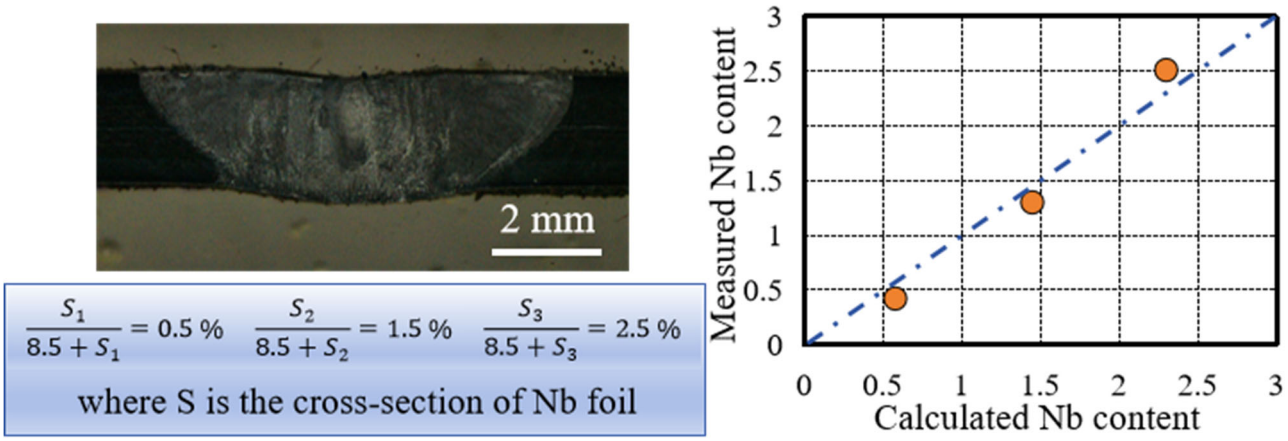

Figure 2. TIG-weld cross-section and Nb content.

Based on the dilution ratio relationship, theoretical calculations indicated that, with an Nb-foil thickness of 0.05 mm, a foil width of 0.85 mm would yield a weld Nb content of 0.5 wt.%, while widths of 2.58 mm and 4.35 mm would correspond to 1.5 wt.% and 2.5 wt.%, respectively. To reduce practical errors, the foil widths were rounded, and the final foil widths introduced for the low-, medium-, and high-Nb welds were 1.0 mm, 2.5 mm, and 4.0 mm, respectively. Based on the designed Nb-foil addition and the dilution analysis, the corresponding nominal Nb contents of the low-, medium-, and high-Nb welds were taken as 0.58 wt.%, 1.45 wt.%, and 2.30 wt.%, respectively. In addition, the weld seam was also tested using a direct reading spectrometer. Figure 2 compares the calculated Nb values

from the dilution rate with those measured by the direct reading spectrometer. It can be seen that the theoretically calculated values are basically consistent with the measured values. Considering that segregation and other phenomena may occur in the prepared weld seam, which will affect the test results, these values are nominal compositions used to represent the three Nb addition levels in the present study.

3.2. Solidification Cracking Susceptibility

The as-fabricated Nb-containing welded joints were ground flush and then machined into trapezoidal specimens for laser-remelting hot-cracking evaluation. Repeated laser-remelting tests were carried out for each Nb-content condition under identical processing parameters to assess the solidification cracking response of the austenitic stainless-steel welds. Two trapezoidal specimen geometries were employed to provide different restraint levels, with a fixed narrow-end width (Ws) of 10 mm and wide-end widths (Wf) of 35 mm and 40 mm.

Figure 3a–d present the macroscopic results of the trapezoidal hot-cracking tests under the present welding conditions and Nb contents, and Figure 3e shows the corresponding critical restraint width. For the 310S/310S austenitic stainless-steel laser welds, the measured critical restraint widths varied within a relatively narrow range under the four Nb conditions. The welds containing 0.58 wt.% Nb and 1.45 wt.% Nb exhibited larger critical restraint widths than the Nb-free and 2.3 wt.% Nb welds. Because a larger critical restraint width generally indicates higher solidification cracking susceptibility, these results suggest that Nb addition affected the cracking response of the weld under the present test conditions.

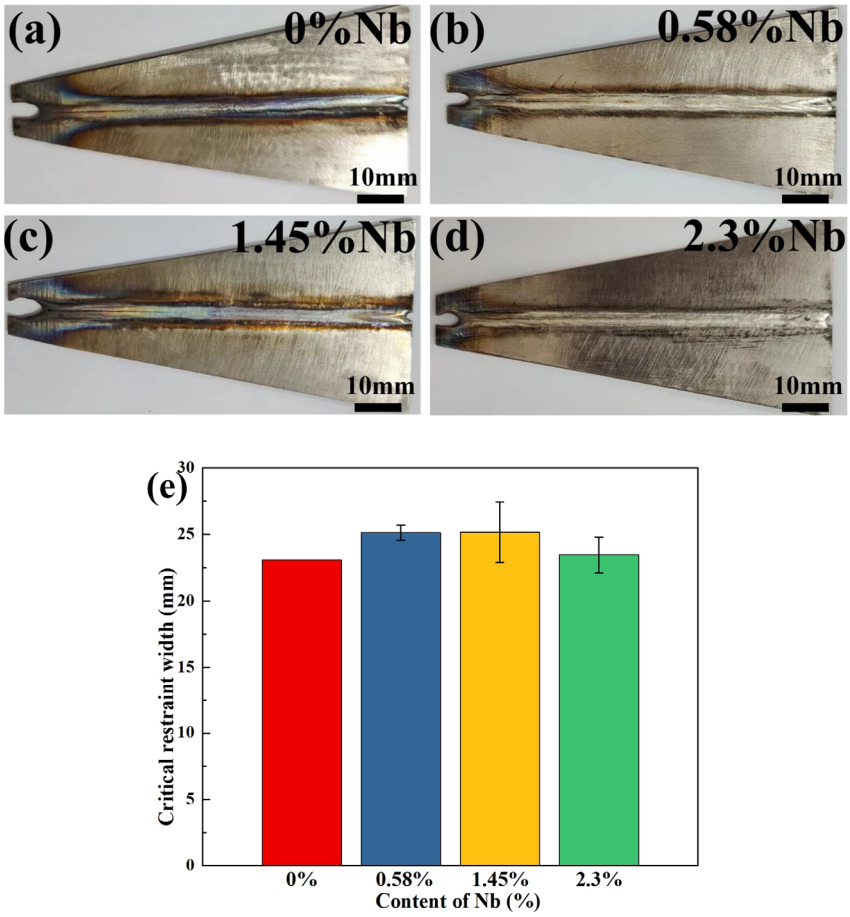

Figure 3. (**a**–**d**) Macroscopic morphology of solidification cracks and (**e**) critical restraint width of laser welds in austenitic stainless-steel with different Nb contents.

Figure 4 shows representative top-surface and cross-sectional macrographs of the laser welds with different Nb contents. All welds exhibited continuous weld beads and full penetration under the present welding conditions. Because full penetration was achieved in all cases, the penetration depth was approximately equal to the sheet thickness, and the characteristic fusion-zone widths in the cross-section are marked directly in the figure. Although some variation in fusion-zone shape was observed among the different Nb contents, the overall weld geometries were comparable.

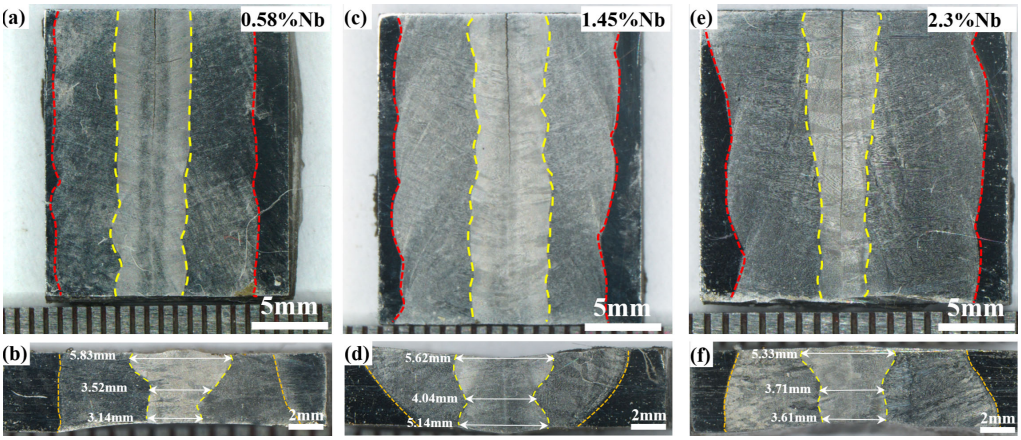

Figure 4. Representative top-surface and cross-sectional macrographs of laser welds with different Nb contents: (**a**,**b**) 0.58 wt.% Nb, (**c**,**d**) 1.45 wt.% Nb, and (**e**,**f**) 2.3 wt.% Nb.

Figure 5 shows the metallographic microstructures on the surface of four austenitic stainless-steel laser welds. As shown in Figure 5a–d, all weld surfaces exhibit an austenitic dendritic morphology; subgrain-boundary features can be identified in the interdendritic regions, and second-phase particles are present in the vicinity of grain boundaries and subgrain boundaries. With increasing Nb content, the number of these second-phase particles in the 310S/310S welds increases markedly, evolving from a small amount of dispersed precipitates to a denser distribution concentrated along grain and subgrain boundaries [25,26]. Meanwhile, both the primary dendrite arm spacing (PDAS) and secondary dendrite arm spacing (SDAS) decrease with increasing Nb content, dropping from 14.92 μm and 4.37 μm to 10.09 μm and 3.67 μm, respectively. The statistical results in Figure 5e are consistent with the microstructural observations, showing that Nb addition reduces the PDAS and SDAS and thereby refines the dendritic substructure of the weld metal. This is mainly because Nb addition promotes the formation of fine, dispersed precipitates in the 310S/310S weld metal. These precipitates may hinder boundary migration to some extent and are likely associated with the refinement of the dendritic substructure, as reflected by the reduced PDAS and SDAS. Such microstructural refinement may contribute to the observed strengthening effect, which becomes more pronounced with increasing Nb content [27].

Figure 6 presents point-EDS analyses of the representative second-phase particles in the microstructures of four austenitic stainless-steel welds, and the results are summarized in Table 4. Figure 6a–d show the SEM morphologies of the welds with 0 wt.% Nb, 0.58 wt.% Nb, 1.45 wt.% Nb, and 2.3 wt.% Nb, respectively. The red circles (P1–P4) indicate representative particle sites selected for analysis, which are mainly located near austenite grain boundaries. Figure 6e–h show the corresponding EDS point spectra of points P1–P4, respectively.

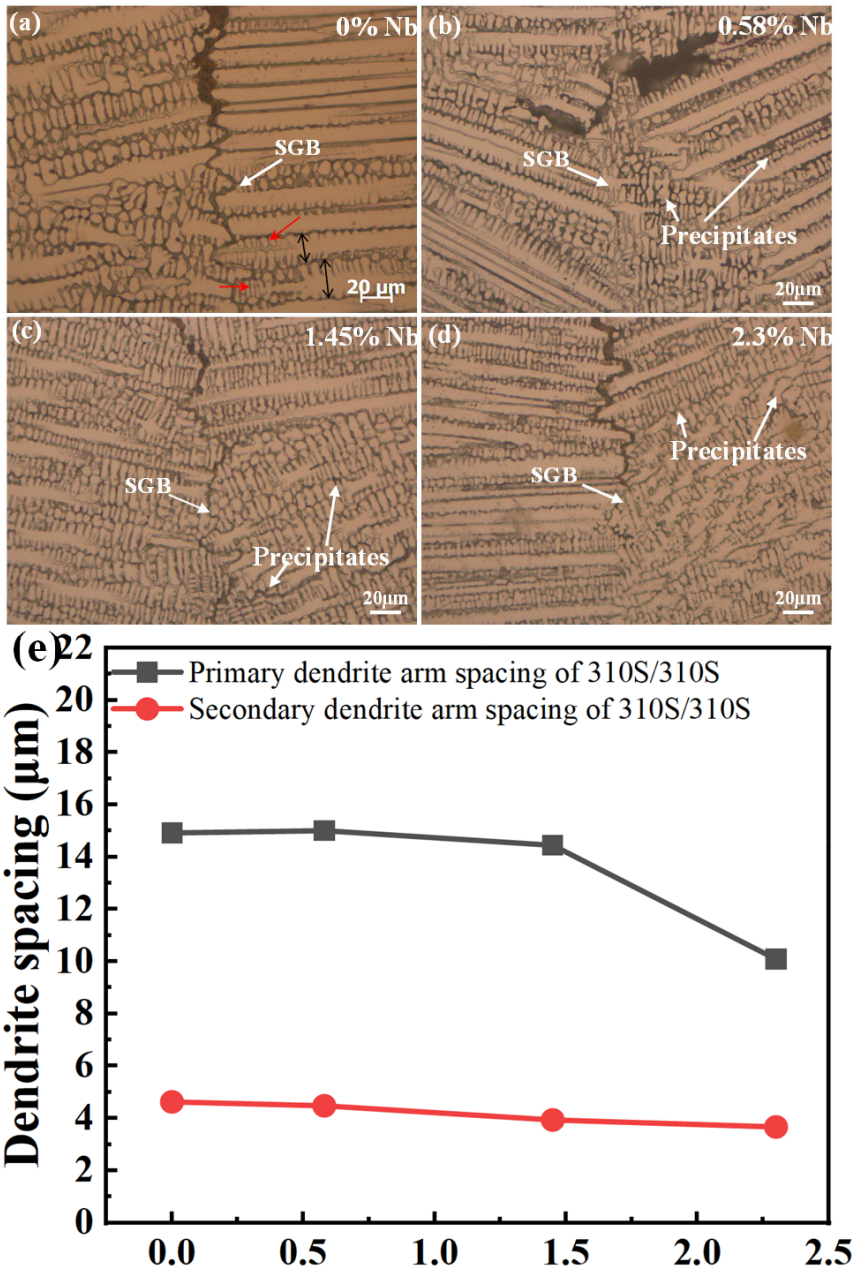

Figure 5. Optical micrographs of the surface of the weld of austenitic stainless-steel: (**a**) 0% Nb; (**b**) 0.58% Nb; (**c**) 1.45% Nb; (**d**) 2.3% Nb; (**e**) statistics of dendrite spacing.

For the Nb-free 310S/310S weld, the precipitate at P1 is likely associated with carbide phases such as $Cr_{23}C_6$, together with other possible constituents. For the Nb-containing welds, the precipitates at P2–P4 show Nb contents mainly in the range of 15–30%, suggesting substantial enrichment of Nb-containing precipitates in these particles. In addition, the C content at P3 is relatively high, indicating that a certain fraction of carbides may also be present at this location. Based on the local EDS results and the relevant literature [15,17], the Nb-containing precipitates mentioned above are considered to be Nb-bearing precipitates and may be associated with phases such as NbC and other Nb-rich constituents; however, specific Fe–Nb intermetallic phases were not directly confirmed by XRD in the present study.

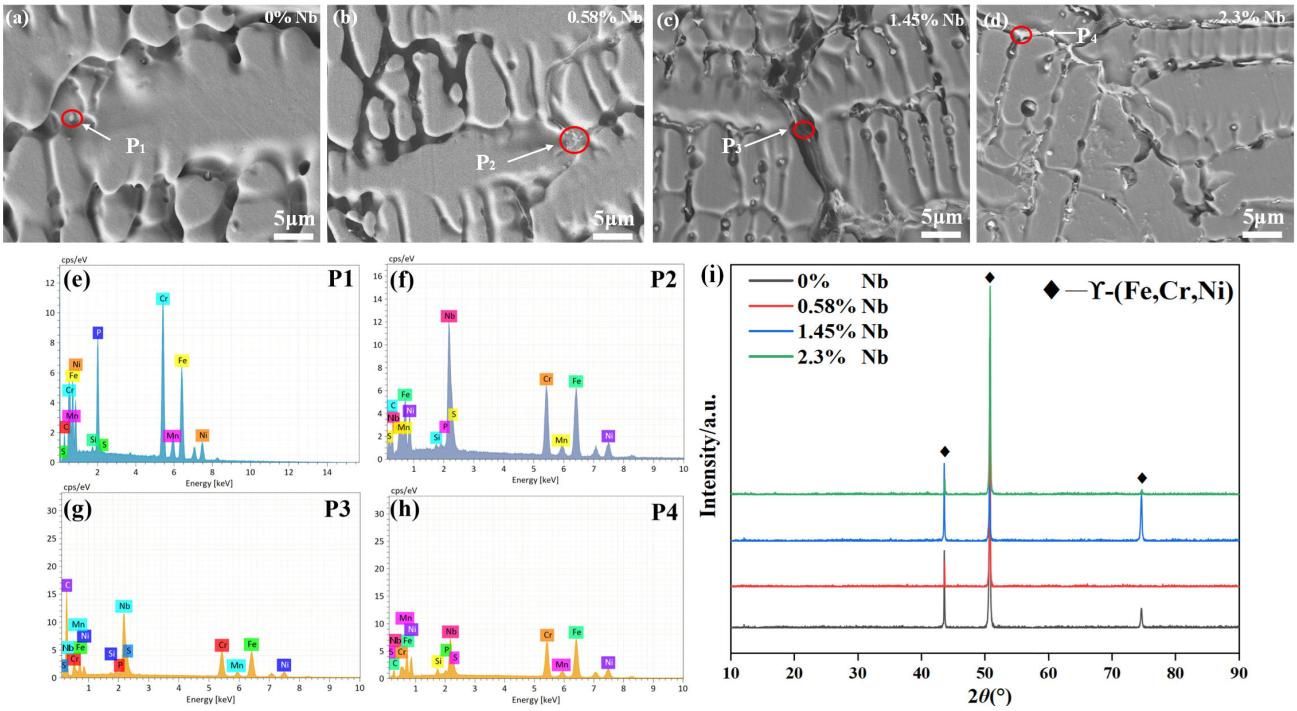

Figure 6. SEM images at the weld center of 310S/310S welds with different Nb contents: (**a**) 0% Nb; (**b**) 0.58% Nb; (**c**) 1.45% Nb; (**d**) 2.3% Nb; (**e**–**h**) EDS point spectra of points P1–P4; (**i**) XRD patterns of welds with different Nb contents.

Table 4. Point EDS results at the marked positions in Figure 6 (wt.%).

Position	C	Fe	Cr	Ni	Nb
P_1	6.95	36.05	34.72	11.91	0
P_2	6.34	33.86	19.33	9.19	30.18
P_3	41.01	19.45	11.12	6.5	21.01
P_4	6.38	36.91	19.76	14.72	18.87

3.3. Mechanical Properties

Figure 7 shows the metallographic microstructures on the transverse cross-sections of the welds with different Nb contents. Figure 7a–d correspond to the welds containing 0 wt.% Nb, 0.58 wt.% Nb, 1.45 wt.% Nb, and 2.3 wt.% Nb, respectively. All optical micrographs were acquired at the same magnification and from equivalent locations on the transverse cross-sections for each condition to ensure a meaningful comparison. The white curve marks the weld centerline. Under all conditions, the weld metal is predominantly austenitic, featuring clearly defined austenitic dendrites with an overall relatively uniform growth orientation. The dendrite growth direction is mostly approximately perpendicular to the weld centerline or forms a certain angle with it. This characteristic is related to the heat-transfer conditions during molten pool solidification. Dendrites typically grow opposite to the direction of heat dissipation; since the temperature gradient normal to the fusion line is larger and the heat is extracted more rapidly, dendrites tend to advance from the molten pool boundary toward the pool center, exhibiting an orientation that is perpendicular to, or slightly inclined relative to, the weld centerline [28]. In addition, precipitates can be observed near the weld centerline at all Nb levels, and they become more pronounced as the Nb content increases. Within this region, these particles are frequently associated with grain boundaries and subgrain boundaries, which is consistent with the

surface observations in Figure 5 and the SEM/EDS results in Figure 6. Meanwhile, the weld microstructure becomes progressively finer with increasing Nb content.

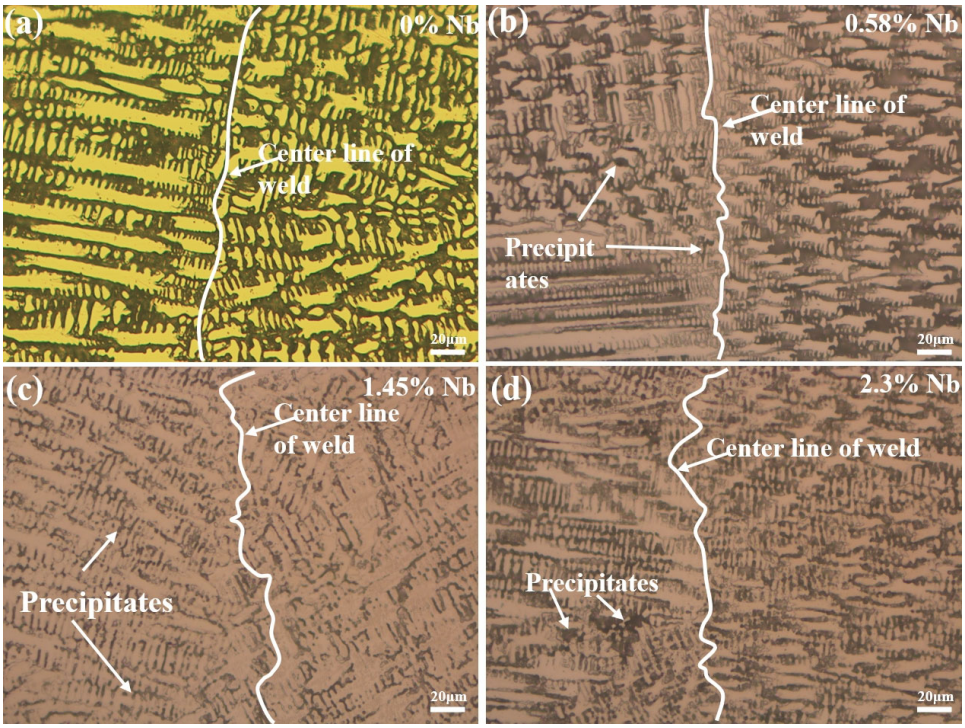

Figure 7. Optical micrographs of laser weld cross-section of austenitic stainless-steel: (**a**) 0%Nb; (**b**) 0.58% Nb; (**c**) 1.45% Nb; (**d**) 2.3% Nb.

The microhardness profile measured along the transverse cross-sections of the welds is shown in Figure 8a. The hardness measurements include the weld metal as well as the adjacent fusion boundary and base-metal regions. An indentation spacing of 0.1 mm was used, and three measurements were performed in each region, with the reported values representing the average results. With increasing Nb content, the overall Vickers hardness of the 310S/310S welds shows an increasing trend, although some local fluctuations are observed at individual measurement points away from the weld centerline. Statistical results indicate that the average Vickers microhardness of the weld metal increases from 110 HV to 173 HV with increasing Nb content. Notably, the microhardness of the weld containing 2.3 wt.% Nb reaches approximately 108% of that of the SUS310S base metal, as shown in Figure 8b. In combination with the microstructural features presented in Figure 7, this increase in microhardness is considered to be mainly associated with refinement of the dendritic substructure, as reflected by the reduced PDAS and SDAS, together with the strengthening effect introduced by Nb. In addition, Nb addition promotes the formation of fine, dispersed Nb-rich precipitates, which may further contribute to the increase in microhardness. Meanwhile, these particles may act as heterogeneous nucleation sites during solidification and thereby contribute to microstructural refinement of the weld metal, which may be beneficial to its mechanical properties [15,17,25]. In addition, although the solubility of Nb in austenite is low, a small amount of Nb can still dissolve into the matrix and pin dislocations via lattice distortion, resulting in a certain degree of solid-solution strengthening [16]. The dispersed precipitates (e.g., NbC) distributed near grain boundaries also contribute to hardness [26]. The non-uniformity in Nb segregation and precipitate distribution can lead to local hardness variations, which explains the observed fluctuations in the hardness profile.

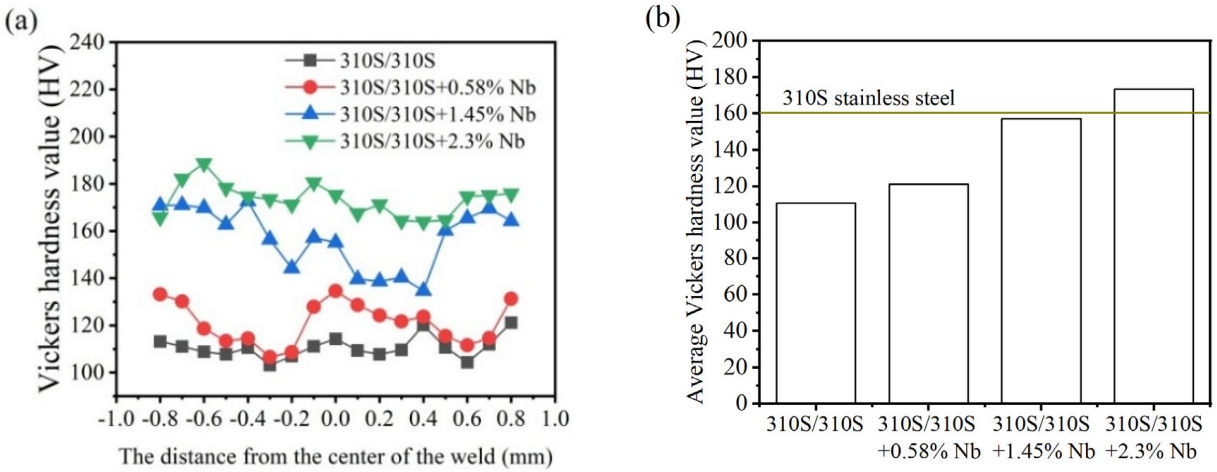

Figure 8. Microhardness on the cross-section of laser weld of 310S/310S with different Nb contents: (**a**) Vickers hardness distribution; (**b**) average Vickers hardness.

The fracture locations after room-temperature tensile testing are shown in Figure 9. When the Nb content is 0 wt.% and 0.58 wt.%, the fractures of the 310S/310S weld specimens mostly occur in the weld center region. When the Nb content increases to 1.45 wt.% and 2.3 wt.%, the fracture location shifts to the weld edge region. This indicates that, with increasing Nb content, the strength of the weld center is enhanced, causing the relatively weak region of the joint to migrate accordingly. For all specimens, the fracture surfaces are approximately perpendicular to the tensile loading direction, and the macroscopic fracture cross-sections exhibit an arc-shaped profile.

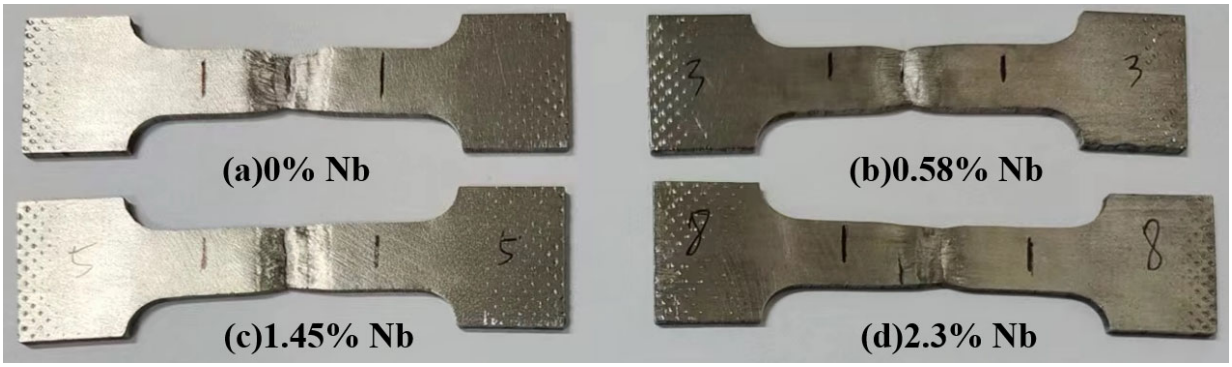

Figure 9. Morphology of austenitic stainless-steel weld specimens after room-temperature tensile testing: (**a**) 0% Nb; (**b**) 0.58% Nb; (**c**) 1.45% Nb; (**d**) 2.3% Nb.

Figure 10 summarizes the tensile behavior of the welds with different Nb contents. Representative engineering stress–strain curves obtained from three tensile tests for each condition are shown in Figure 10a, and the corresponding section shrinkage values are presented in Figure 10b. As the Nb content increases from 0 to 2.3 wt.%, the ultimate tensile strength of the 310S/310S laser weld increases from 477.35 MPa to 556.65 MPa, reaching 92.4% of that of the 310S base metal. The reduction in area (section shrinkage), determined locally at the final fracture region from the minimum residual cross-sectional area after tensile failure, reaches a maximum of 57.9% at 0.58 wt.% Nb, while remaining approximately stable at (50 ± 2)% for the other Nb contents.

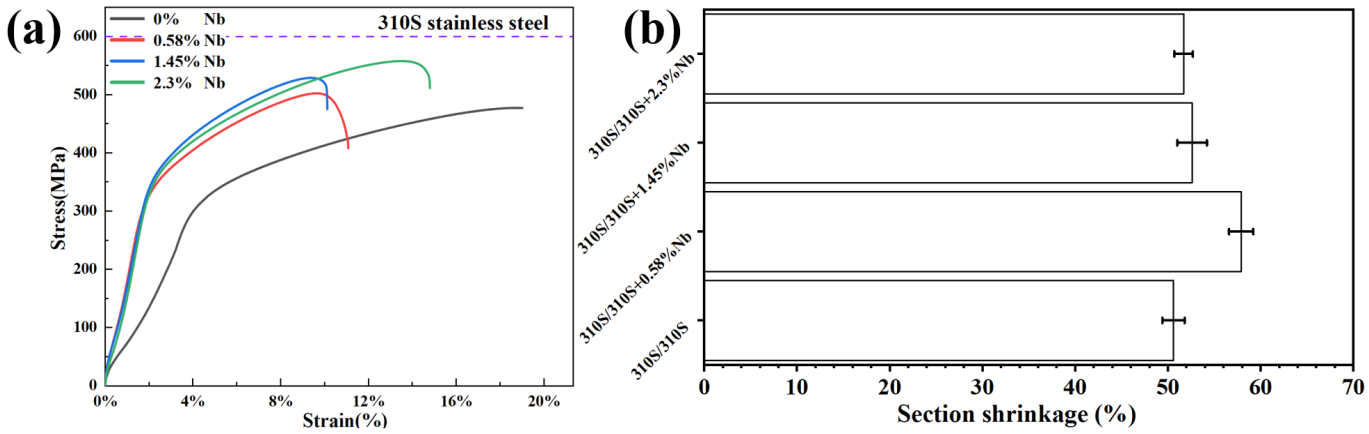

Figure 10. (**a**) Stress–strain curves of laser-welded Nb-containing austenitic stainless-steel; (**b**) reduction in area of laser-welded section of Nb-containing austenitic stainless-steel.

The increase in tensile strength is mainly associated with the microstructural refinement induced by Nb addition, as reflected by the reductions in PDAS and SDAS, together with the strengthening effect introduced by Nb-rich precipitates [29]. The refined dendritic/cellular substructure and the dispersed precipitates can increase the resistance to dislocation motion, thereby enhancing the strength of the weld metal. Meanwhile, at relatively low Nb contents, such microstructural refinement may promote more-uniform local deformation, which is beneficial to ductility. However, when the Nb content is further increased, the increased amount of Nb-rich precipitates may reduce deformation compatibility and thus impair ductility. On the other hand, lattice distortion caused by the atomic size mismatch between Nb and Fe can hinder dislocation motion, providing a certain degree of solid-solution strengthening; however, it may also increase resistance to plastic deformation and thus be detrimental to ductility [16]. These hard and brittle phases can promote stress concentration at their interfaces with the matrix and act as potential crack initiation sites during tensile deformation [26]. Considering the combined effects of refinement of the dendritic substructure, solid-solution strengthening, and the formation of FeNb (σ phase) and Fe_2Nb-type Laves phase, the weld strength continues to increase with increasing Nb content, whereas the ductility improves at 0.58 wt.% Nb and then decreases as Nb is further increased, resulting in a trend where the reduction in area first increases and then decreases.

The fracture morphology is shown in Figure 11. The fractures of each weld are predominantly characterized by a large number of conical dimples, exhibiting typical ductile fracture features overall. As the Nb content increases, the size of the dimples generally enlarges while their number decreases, and larger precipitates can be observed under low magnification in Figure 11. In the fractures with 0 and 0.58 wt.% Nb, locally flat regions with indistinct dimple features are present. When the Nb content reaches 1.45 wt.%, scattered secondary phase particles appear at the bottom of some dimples in Figure 11c; such particles are prone to induce localized stress concentration, promoting microcrack initiation and facilitating crack propagation. As the Nb content further increases to 2.3 wt.%, the dimple morphology becomes elongated; the dimple walls thicken, and the traces of plastic deformation diminish, indicating a reduction in the local plastic energy dissipation capacity during the fracture process.

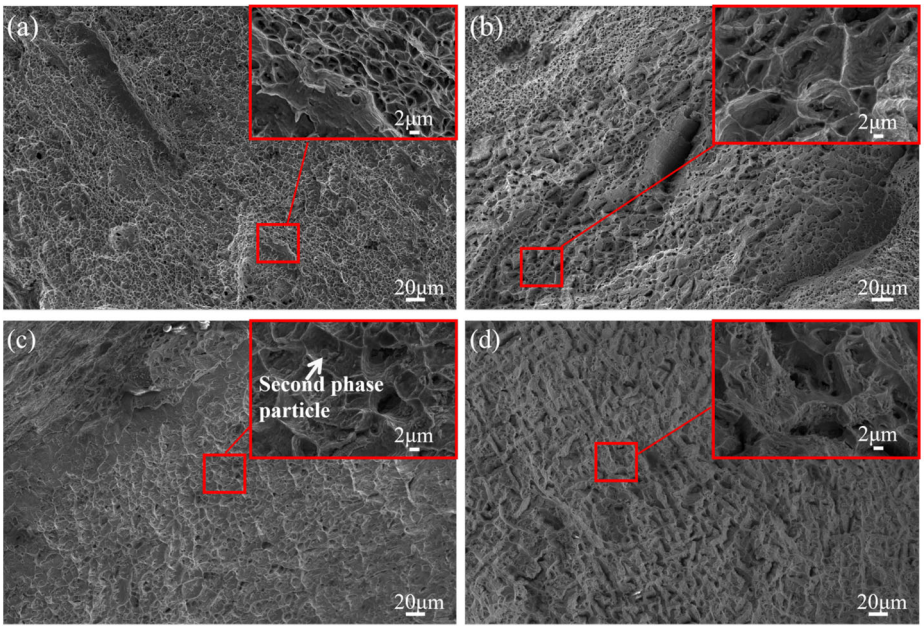

Figure 11. Tensile fracture morphology of laser weld of austenitic stainless-steel at room temperature: (**a**) 0% Nb; (**b**) 0.58% Nb; (**c**) 1.45% Nb; (**d**) 2.3% Nb.

3.4. Corrosion Resistance

To quantitatively evaluate the intergranular corrosion (IGC) resistance of the austenitic stainless-steel laser welds, the welds were characterized by the double-loop electrochemical potentiokinetic reactivation (DL-EPR) test. The basic principle of the DL-EPR test is as follows: in an acidic electrolyte, the specimen is first subjected to a forward potentiodynamic scan, during which the material gradually transitions from active dissolution to a passive state and forms a passive film; the maximum anodic current density, Ia, is obtained during this process. The potential is then scanned back at the same rate into the reactivation region. If the weld has been sensitized by the welding thermal cycle, for example, through grain-boundary carbide precipitation leading to Cr depletion at grain boundaries, the Cr-depleted regions exhibit weaker passivation/repassivation capability and preferentially undergo selective dissolution during the reverse scan, giving rise to a reactivation current peak, Ir. The ratio Ir/Ia is commonly used to indicate IGC susceptibility; a larger Ir/Ia implies a stronger reactivation tendency under the present test conditions and thus a higher IGC susceptibility [30].

The DL-EPR curves of the welds with four different Nb contents are shown in Figure 12. Figure 13 summarizes the representative Ir/Ia values obtained under the same test conditions for the weld longitudinal sections. The maximum reactivation current densities Ir for the 0 wt.% Nb, 0.58 wt.% Nb, 1.45 wt.% Nb, and 2.3 wt.% Nb welds are 0.01226, 0.01297, 0.01140, and 0.00944 A/cm^2, respectively; the corresponding maximum anodic current densities Ia are 0.01814, 0.02157, 0.02044, and 0.01808 A/cm^2, respectively. Although statistical scatter is not provided in the present work, the Ir/Ia value of the 310S/310S laser weld decreases progressively from 67.6% to 52.2% with increasing Nb content, suggesting that increasing Nb content reduces the reactivation tendency under the present DL-EPR test conditions and improves the weld's resistance to intergranular corrosion.

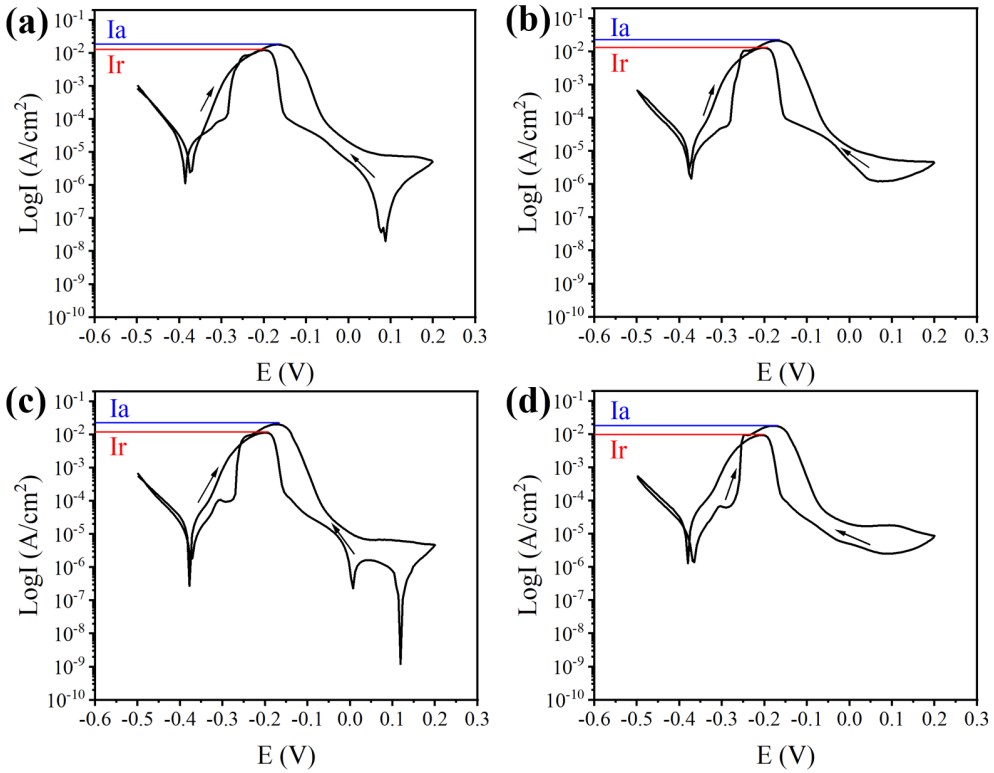

Figure 12. DL-EPR curves of laser weld of four austenitic stainless-steels: (**a**) 0% Nb; (**b**) 0.58% Nb; (**c**) 1.45% Nb; (**d**) 2.3% Nb.

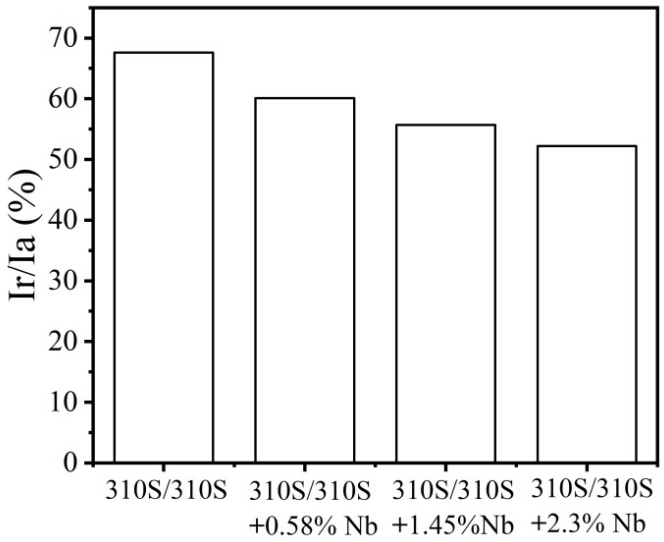

Figure 13. Representative Ir/Ia ratios of 310S/310S laser welds with different Nb contents.

This may be attributed to the fact that, during welding, Nb preferentially combines with free carbon to form MC-type (Nb-rich) carbides, thereby stabilizing carbon and suppressing the precipitation of Cr carbides at grain boundaries. As a result, the degree of Cr depletion at grain boundaries is alleviated, and the connectivity of Cr-depleted regions is reduced, ultimately improving the intergranular corrosion behavior of the weld [31].

The metallographic morphologies of the weld longitudinal sections after the DL-EPR test are shown in Figure 14. The microstructure exhibits an alternating distribution of bright and dark regions. These regions more reasonably reflect different degrees of surface attack after the DL-EPR test. The darker areas correspond to regions that underwent more-severe local dissolution, whereas the brighter areas indicate relatively less-pronounced attack.

This selective dissolution is typically associated with defects such as grain boundaries and subgrain boundaries. As observed in the high-magnification images in Figure 14b,d,f,h, subgrain-boundary features can be identified, indicating that, in addition to grain boundaries, local subgrain boundaries may also act as preferential dissolution pathways under the present test conditions. Combined with the Ir/Ia results, it can be inferred that, with increasing Nb content, the local reactivation tendency of these preferentially dissolved regions decreases and the tendency for selective corrosion at grain boundaries and their adjacent areas is weakened. This trend is consistent with the reduced intergranular corrosion susceptibility indicated by the decreasing Ir/Ia ratio.

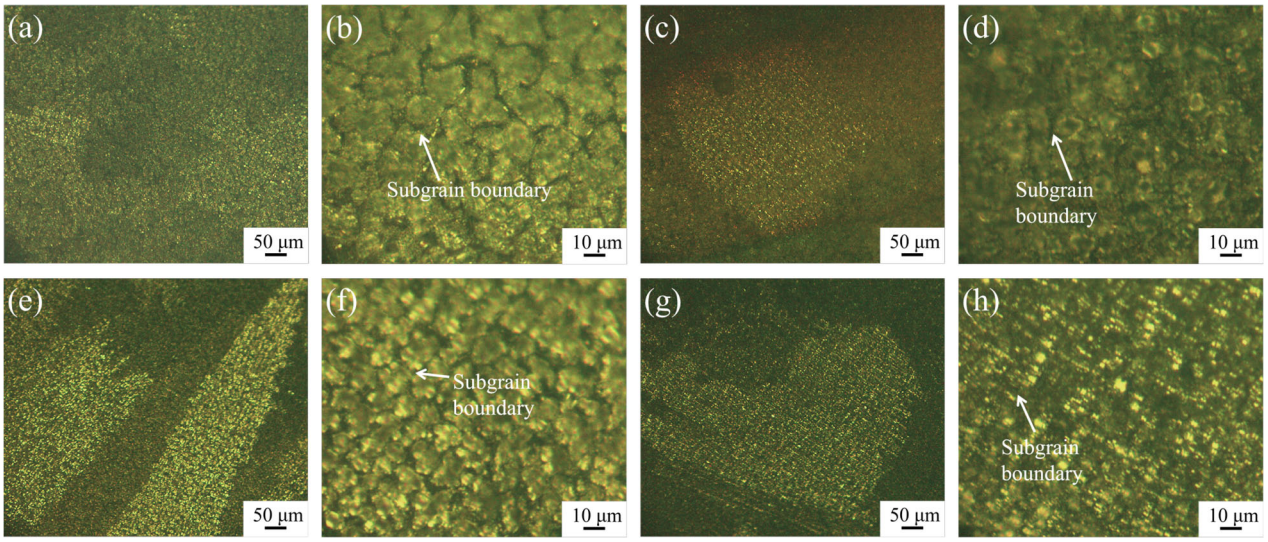

Figure 14. Optical micrographs of weld longitudinal sections after the DL-EPR test for 310S/310S laser welds with different Nb contents: (**a**) 0% Nb (310S/310S); (**b**) higher-magnification view of (**a**); (**c**) 0.58% Nb; (**d**) higher-magnification view of (**c**); (**e**) 1.45% Nb; (**f**) higher-magnification view of (**e**); (**g**) 2.3% Nb; (**h**) higher-magnification view of (**g**).

4. Conclusions

In the present study, Nb addition significantly affected the solidification cracking behavior, microstructure, mechanical properties, and intergranular corrosion resistance of 310S/310S laser welds. Under the present experimental conditions, the critical restraint width increased from 23.08 mm to a maximum of 25.16 mm and then decreased to 23.46 mm with increasing Nb content, indicating that moderate Nb addition produced the highest solidification cracking susceptibility. SEM/EDS observations showed that increasing Nb content promoted the formation of Nb-rich second-phase particles, mainly near austenite grain boundaries, and enhanced Nb enrichment in grain-boundary regions. These observations suggest that Nb segregation is an important microstructural factor affecting both precipitation behavior and the cracking/plasticity response of the weld metal. Mechanical testing showed that Nb addition increased the average microhardness from 110 HV to 173 HV and the tensile strength from 477.35 MPa to 556.65 MPa, while the reduction in area first increased and then decreased. This trend suggests that low Nb addition improved the strength–ductility balance, whereas excessive Nb may have reduced plasticity because of the increased presence of Nb-rich phases and stronger solid-solution strengthening. In addition, the Ir/Ia ratio decreased from 67.6% to 52.2% with increasing Nb content, indicating a reduced degree of sensitization and improved intergranular corrosion resistance. This improvement is likely related to the preferential reaction of Nb with carbon, which may suppress the formation of Cr-depleted zones at grain boundaries.

Author Contributions: Conceptualization, Y.S., D.W. and X.W.; methodology, Y.S., D.W. and X.W.; data curation, Y.S., D.W. and X.W.; visualization, D.W. and X.W.; validation, D.W. and X.W.; formal analysis, Y.S., D.W. and X.W.; investigation, Y.S., D.W. and X.W.; resources, D.W. and X.W.; writing—original draft preparation, Y.S.; writing—review and editing, Y.S., D.W. and X.W.; project administration, D.W. and X.W.; supervision, D.W. and X.W. All authors have read and agreed to the published version of the manuscript.

Funding: This research received no external funding.

Data Availability Statement: The original contributions presented in this study are included in the article. Further inquiries can be directed to the corresponding authors.

Conflicts of Interest: The authors declare no conflicts of interest.

References

1. Soltani, H.M.; Tayebi, M. Comparative Study of AISI 304L to AISI 316L Stainless Steels Joints by TIG and Nd:YAG Laser Welding. *J. Alloys Compd.* **2018**, *767*, 112–121. [CrossRef]
2. Guo, Y.; Sun, Z.; Guo, S.; Fu, J. Research on a Novel Heat Treatment Process for Boron Steel Used for Soil-Engaging Components of Tillage Machinery. *Agriculture* **2024**, *14*, 1555. [CrossRef]
3. Hong, K.-M.; Shin, Y.C. Prospects of Laser Welding Technology in the Automotive Industry: A Review. *J. Mater. Process. Technol.* **2017**, *245*, 46–69. [CrossRef]
4. Assunção, E.; Quintino, L.; Miranda, R. Comparative Study of Laser Welding in Tailor Blanks for the Automotive Industry. *Int. J. Adv. Manuf. Technol.* **2010**, *49*, 123–131. [CrossRef]
5. Wang, L.; Zhang, G.; Xu, J.; Li, Y.; Chen, Q.; Rong, Y.; Huang, Y. Effect of Collapse and Hump on Thermomechanical Behavior in High-Power Laser Welding of 16-mm Marine Steel EH40. *Int. J. Adv. Manuf. Technol.* **2022**, *120*, 2003–2013. [CrossRef]
6. Xia, H.; Li, L.; Tan, C.; Yang, J.; Li, H.; Song, W.; Zhang, K.; Wang, Q.; Ma, N. In Situ SEM Study on Tensile Fractured Behavior of Al/Steel Laser Welding-Brazing Interface. *Mater. Des.* **2022**, *224*, 111320. [CrossRef]
7. Xia, H.; Yang, B.; Su, J.; Liu, Y.; Su, X.; Wang, C.; Qiang, X.; Wu, T.; Tan, C. Improvement of Laser Welded TC4/CFRTP Joint Strength by Combination of Surface Modification of MAO and Laser Texturing. *Thin-Walled Struct.* **2024**, *196*, 111409. [CrossRef]
8. Ai, Y.; Wang, Y.; Yan, Y.; Han, S.; Huang, Y. The Evolution Characteristics of Solidification Microstructure in Laser Welding of Ti-6Al-4V Titanium Alloy by Considering Transient Flow Field. *Opt. Laser Technol.* **2024**, *170*, 110195. [CrossRef]
9. Yan, J.; Gao, M.; Zeng, X. Study on Microstructure and Mechanical Properties of 304 Stainless Steel Joints by TIG, Laser and Laser-TIG Hybrid Welding. *Opt. Lasers Eng.* **2010**, *48*, 512–517. [CrossRef]
10. Yu, X.; Long, Q.; Chen, Y.; Liu, Y.; Yang, C.; Jia, Q.; Wang, C. Laser Transmission Welding of Dissimilar Transparent Thermoplastics Using Different Metal Particle Absorbents. *Opt. Laser Technol.* **2022**, *150*, 108005. [CrossRef]
11. Sfregola, F.A.; De Palo, R.; Gaudiuso, C.; Patimisco, P.; Ancona, A.; Volpe, A. Femtosecond Laser Transmission Joining of Fused Silica and Polymethyl Methacrylate. *Macromol. Mater. Eng.* **2025**, *310*, 2400354. [CrossRef]
12. Ding, Z.; Tang, Z.; Zhang, B.; Ding, Z. Vibration Response of Metal Plate and Shell Structure under Multi-Source Excitation with Welding and Bolt Connection. *Agriculture* **2024**, *14*, 816. [CrossRef]
13. Ueda, S.; Kadoi, K.; Tokita, S.; Inoue, H. Relationship between Alloy Element and Weld Solidification Cracking Susceptibility of Austenitic Stainless Steel. *ISIJ Int.* **2019**, *59*, 1323–1329. [CrossRef]
14. Hosseini, H.S.; Shamanian, M.; Kermanpur, A. Microstructural and Weldability Analysis of Inconel617/AISI 310 Stainless Steel Dissimilar Welds. *Int. J. Press. Vessel. Pip.* **2016**, *144*, 18–24. [CrossRef]
15. Burja, J.; Tome, S.; Nagode, A. Temperature-Dependent Effectiveness of Ti, Nb, Zr, and Y in Controlling Grain Growth of AISI 304 Austenitic Stainless Steel. *Crystals* **2025**, *15*, 931. [CrossRef]
16. Chen, J.; Ren, J.-k.; Liu, Z.-y.; Wang, G.-d. The Essential Role of Niobium in High Manganese Austenitic Steel for Application in Liquefied Natural Gas Tanks. *Mater. Sci. Eng. A* **2020**, *772*, 138733. [CrossRef]
17. Liu, X.; Wang, H.; Liu, Y.; Wang, C.; Song, Q.; Cui, H.; Zhang, C.; Huang, K. The Effect of Nb Content on Microstructure and Properties of Laser Cladding 316L SS Coating. *Surf. Coat. Technol.* **2021**, *425*, 127684. [CrossRef]
18. Kumar, M.S.; Gopi, S.; Sivashanmugam, N.; Sasikumar, A. A Study on Corrosion Behavior of Stainless Steel Dissimilar Alloy Weld Joints (321 & 347). *Mater. Today Proc.* **2021**, *46*, 9229–9231. [CrossRef]
19. Frankel, G. Pitting Corrosion of Metals: A Review of the Critical Factors. *J. Electrochem. Soc.* **1998**, *145*, 2186–2198. [CrossRef]
20. Dulieu, D. The Role of Niobium in Austenitic and Duplex Stainless Steels. In Proceedings of the International Symposium on Niobium 2001, Orlando, FL, USA, 14–17 October 2001; pp. 975–999.
21. Wang, W.; Xiong, L.; Wang, D.; Ma, Q.; Hu, Y.; Hu, G.; Lei, Y. A New Test Method for Evaluation of Solidification Cracking Susceptibility of Stainless Steel during Laser Welding. *Materials* **2020**, *13*, 3178. [CrossRef]

22. Wang, D.; Zhang, F.; Warinsiriruk, E.; Zhu, Q.; Li, T.; Li, H.; Xu, N.; Han, K.; Wang, Z.; Yang, S. A Novel Method for Evaluating Solidification Cracking Susceptibility of Austenitic Stainless Steel Using Trapezoidal Hot Cracking Test during Laser Welding. *Opt. Laser Technol.* **2024**, *175*, 110789. [CrossRef]
23. *GB/T 2651-2008*; Tensile Test Method on Welded Joints. Standards Press of China: Beijing, China, 2008.
24. Luo, X.; Fang, K.; Zhang, W.; Zhang, J.; Yang, X.; Liu, X.; Zha, X.; Zhang, X. Effect of Tempering Temperature on Microstructure and Intergranular Corrosion Property of 2205 Duplex Stainless Steel. *Coatings* **2024**, *14*, 776. [CrossRef]
25. Jeng, S.-L.; Lee, H.-T.; Huang, J.-Y.; Kuo, R.-C. Effects of Nb on the Microstructure and Elevated-Temperature Mechanical Properties of Alloy 690-SUS 304L Dissimilar Welds. *Mater. Trans.* **2008**, *49*, 1270–1277. [CrossRef]
26. Padilha, A.F.; Machado, I.F.; Plaut, R.L. Microstructures and Mechanical Properties of Fe–15% Cr–15% Ni Austenitic Stainless Steels Containing Different Levels of Niobium Additions Submitted to Various Processing Stages. *J. Mater. Process. Technol.* **2005**, *170*, 89–96. [CrossRef]
27. Okayasu, M.; Wu, S.; Noda, K.; Lin, D.-Y.; Yang, S.-M. Mechanical Properties of Austenitic Stainless Steel with High Niobium Contents. *Mater. Sci. Technol.* **2016**, *32*, 1382–1394. [CrossRef]
28. Lippold, J.C. *Welding Metallurgy and Weldability*; John Wiley & Sons: Hoboken, NJ, USA, 2014. [CrossRef]
29. Wang, F.; Xiao, G.; Ma, J.; Wang, N.; Song, B.; Qiang, Y.; Huang, D.; Zou, D. Effect of Niobium Content on Microstructure and Mechanical Properties of AISI 304N Austenitic Stainless Steel. *Mater. Sci. Eng. A* **2025**, *891*, 149103. [CrossRef]
30. Altamirano, P.M.; Kappes, M.A.; Rodríguez, M.A. In-Situ Determination of the Degree of Sensitization in Austenitic Stainless Steels by DL-EPR. In Proceedings of the NACE CORROSION 2022 Conference, Houston, TX, USA, 13–17 March 2022; pp. 1–15. [CrossRef]
31. Bai, G.; Lu, S.; Li, D.; Li, Y. Influences of Niobium and Solution Treatment Temperature on Pitting Corrosion Behaviour of Stabilised Austenitic Stainless Steels. *Corros. Sci.* **2016**, *108*, 111–124. [CrossRef]